SICT 2024 Intl. Conference

April 17 to 19, 2024, Vienna, Austria

Conference Proceedings

DOI:

https://doi.org/10.26799/cp-sict-2024

Proceedings of the SICT 2024 International Conference
Vienna, Austria – April 17 – 19, 2024
DOI: https://doi.org/10.26799/cp-sict-2024

Investigation of Thermal and Mechanical Properties of Ti-Si-B-C Nanocomposite Coatings

A. Thewes [1*], L. Bröcker[1], P.M. Reinders [1,2], H. Paschke [2], T. Brückner [2], C. Sternemann [3], M. Paulus [3], W. Tillmann [4], J. Urbanczyk [4], N.F. Lopes Dias [4]
[1] TU Braunschweig, Institute for Surface Technology, Braunschweig, Germany
[2] Fraunhofer Institute for Surface Engineering and Thin Films IST, Braunschweig, Germany
[3] Technische Universität Dortmund, Fakultät Physik/DELTA, Dortmund, Germany
[4] TU Dortmund, Institute of Materials Engineering, Dortmund, Germany

Abstract

Nanocomposite Ti-Si-B-C coatings were analyzed regarding their hardness, fracture toughness, and oxidation resistance. These coatings were deposited by plasma enhanced chemical vapor deposition (PECVD). Self-organization during coating deposition leads to a nanocomposite coating structure, consisting of nanocrystalline TiC grains embedded in an amorphous matrix. This coating system was deposited on nitride AISI H11 hot working steel with a TiN interlayer and offered good adhesion (HF2). With a hardness of 29.2 GPa, the coating system is a possible candidate for application as a wear reducing coating on a tool surface. In view of the harsh environment in many tribological applications in hot forming or molding, the thermal stability and oxidation resistance are of special interest. *In-situ* X-ray diffraction analysis at elevated temperatures showed the beginning of TiO_2 formation at 800 °C, marking it as the starting point for oxidation. With an increase in temperature, the TiO_2 reflexes get stronger, but (200) TiC remains the strongest reflex.

1. Introduction

In hot forming applications, e.g. hot extrusion of copper, severe wear on tool surfaces increases production costs of semi-finished products like bars, pipes, and wires [1]. Research and development of hard and thermally stable Ti-Si-B-C nanocomposite coatings is an approach to realize a wear protective coating. PECVD is a technology which enables the deposition of a homogeneous coating even on complex geometries of tools. For example, in hot extrusion, wear mechanisms are active on the face of the extrusion die and inside the channel.

The nanocomposite coatings consist of nanocrystalline (nc-) grains embedded in an amorphous (a-) matrix. Those nanostructured materials are well understood for Ti-Si-N [2–5] and Ti-B-N [6–9] coatings. Investigation of N-free nanocomposite coatings based on refractory metal Ti was met with less effort. The research group around Mahato *et al.* published several research papers on Ti-Si-B-C nanocomposite coatings [10–17]. However, no independent investigators have verified those results, especially not by coating deposition experiments and extensive analysis by material characterization. This article is considering the works of Mahato *et al.* while simultaneously delivering novel results on Ti-Si-B-C coatings.

Experimental details

The coating deposition was carried out in a PECVD coating deposition device by Rübig with a precedent one hour plasma etching and one hour plasma nitriding step, as described elsewhere [18]. Substrate material was AISI H11 hot working steel. Coating deposition started with TiN for adhesion improvement and gradually changed within 1.5 h by linearly decrease of N_2 flow rate to zero and increase in BCl_3 and tetramethylsilane (TMS) flow. The second part of coating deposition was 4.5 h in which coating composition and gaseous atmosphere was kept nearly constant to create a homogeneous chemical composition close to the surface. The gas flow parameters were 200 L/h H_2, 4.6 L/h $TiCl_4$, 6 L/h Ar, with BCl_3 and TMS ramped up from 8 to 12 L/h and from 3.2 to 4.0 L/h, respectively. During deposition, pressure was maintained at a constant level of 200 Pa and temperature at 530 °C. Voltage was increased in the first 1.5 h from 510 V to 560 V and kept constant at 560 V during 4.5 h step.

Electron probe micro analysis was used to determine the chemical composition of Ti-Si-B-C, including residual Cl and O, which are incorporated in the coating during deposition. Coating characterization implied methods for analysis of mechanical and thermal properties. Hardness was measured by means of nanoindentation in accordance with Zak *et al.* [19]. X-ray diffraction experiments at BL9 at the

DOI: https://doi.org/10.26799/cp-sict-2024

synchrotron radiation source DELTA in Dortmund [20] gave evidence of crystalline phases in the coating. Those experiments were carried out in ambient air at room temperature, 800 °C, 850 °C, 875 °C, and 900 °C to compare the as-deposited state with the oxidized one. Beam size was 1.5 mm in width and 0.2 mm in height, using a photon energy of 13 keV and an angle of incidence of 1°. Raman spectroscopy gives evidence of amorphous a-C(:H). A DXR2 Raman Microscope (Thermo Fisher Scientific, Germany) with a laser wavelength of 532 nm, a laser power of 6 mW and a 50 µm slit was used with 100 exposures for 5 s.

2. Results

The chemical composition was 25.7 at.-% Ti, 12.4 at.-% Si, 20.1 at.-% B, 37.5 at.-% C, 2.2 at.-% O and 2.1 at.-% Cl, resulting in a hardness of 29.2 ± 2.4 GPa. The results of the X-ray diffraction experiments are shown in fig. 1. In the as deposited state, only (200) and (202) TiC was observed. Comparing the relative peak intensity, the (200) TiC reflex is significantly stronger pronounced. At temperatures between 800 °C and 900 °C, both TiC reflexes can still be observed, with a slight decrease in intensity with increasing temperature. At 800 °C, (110), (101), (211), (220), and (301) rutile is observed by weakly pronounced characteristic reflexes. Those reflexes intensify with increasing temperature.

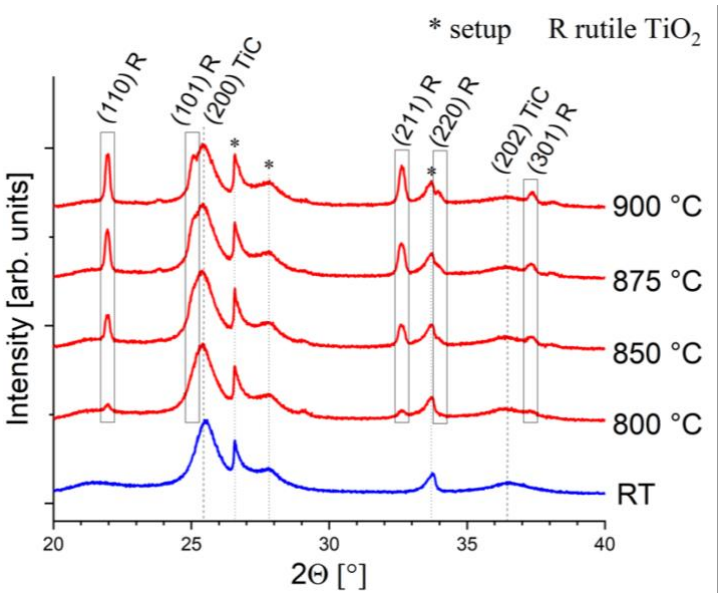

Fig. 1: *In-situ* X-ray diffraction patterns of Ti-Si-B-C at different temperature levels in ambient air

The Raman spectrum is given in fig. 2. The Raman shift of 1000 to 1800 cm^{-1} is shown, because D and G band configuration are identified at 1360 and 1580 cm^{-1}, respectively. The broad double peak proves, that the high C content (37.5 at.-%) led to formation of a-C(:H) phases. Those results are comparable to other nanocrystalline coatings, e.g. Ti-Si-C-N [21] and Ti-B-C-N [22]. In addition, Mahato *et al.* published similar Raman spectra for their nanocomposite Ti-Si-B-C coatings [11].

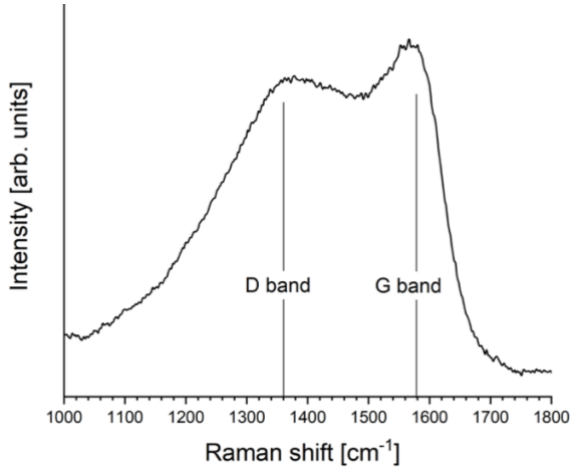

Fig. 2: Raman spectrum of Ti-Si-B-C coating to identify D and G band configurations

DOI: https://doi.org/10.26799/cp-sict-2024

3. Discussion

Despite their numerous valuable contributions to the research of Ti-Si-B-C nanocomposite coatings, Mahato *et al.* never analyzed the behavior of TiC grains during oxidation [11]. The center of attention is in the question, whether TiO_2 phase is formed as rutile, anatase, or both. The oxidation behavior observed in this study is consistent with the results published by Moritz *et al.* for Ti-Si-N coatings [3]. They found, that oxidation of TiN in nanocomposite coatings led to formation of rutile phase instead of anatase and marked the beginning of formation of anatase at approximately 920 °C, where rutile and anatase coexist. Instead of TiN, TiC was oxidized in the Ti-Si-B-C coating, but as oxidation resistance and crystal structure of TiN and TiC are comparable, the oxidation process appears to be of comparable nature, meaning that up to 900 °C, only rutile phase is formed.
The observation of both TiC and rutile is no contradiction in itself. At the top of the coating, O_2 reaches the TiC grains and oxidizes them to form rutile. Beneath, the Si-containing a-matrix hinders oxidation of grains by surrounding and protecting them as well as acting as a diffusion barrier to oxygen. In conclusion, the X-ray diffraction results are a superposition of an oxide top layer containing rutile crystals and an as-deposited nanocomposite structure with crystalline TiC.

4. Conclusions

The coating exhibits a nanocomposite structure, as evidenced by the existence of small, crystalline grains by X-ray diffraction experiments and a-matrix by observation of a-C(:H) in Raman spectra. Coating hardness is limited to 29.2 GPa instead of exceeding 40 GPa to be classified as super hard. This is probably due to relatively high amounts of oxygen (2.2 at.-% in as-deposited state) that was incorporated during coating deposition. Reduction of oxygen residuals during oxidation might be the only way to significantly increase the hardness. Oxidation of coatings started at 800 °C with minor traces of rutile. The intensity of rutile reflexes in X-ray diffraction patterns continually increased with higher temperature, while the TiC reflexes decreased in intensity. In summary, the crystalline TiC chemically reacts with air and forms gaseous CO_x and solid, crystalline TiO_2 as rutile.

Acknowledgements

The authors would like to thank DELTA for providing the synchrotron radiation at beamline BL9 and the support of the German Research Foundation (DFG) within the projects No. 434108570 and INST 212/330-1, project No. 619186. The research project No. 22603 of the research association “Stifterverband Metalle e.V.” has been financially supported within the program of the “Industrielle Gemeinschaftsforschung” (IGF) by the “Bundesministerium fuer Wirtschaft und Klimaschutz” (BMWK) via the DLR. We are thankful for the assistance given.

References

1. Thewes, P. M. Reinders, H. Paschke, T. Brückner, D. Templin, S. Lechner, S. Müller, M. Paulus, C. Sternemann, Surface modifications to reduce wear in hot extrusion of copper, *Wear* 548-549, 205358 (2024); doi: 10.1016/j.wear.2024.205358.
2. M. Diserens, J. Patscheider, F. Lévy, Improving the properties of titanium nitride by incorporation of silicon, *Surface & Coatings Technology*, 241–246 (1998).
3. Y. Moritz, C. Saringer, M. Tkadletz, A. Stark, N. Schell, I. Letofsky-Papst, C. Czettl, M. Pohler, N. Schalk, Oxidation behavior of arc evaporated TiSiN coatings investigated by in-situ synchrotron X-ray diffraction and HR-STEM, *Surface and Coatings Technology* 404, 126632 (2020); doi: 10.1016/j.surfcoat.2020.126632.
4. F. Movassagh-Alanagh, A. Abdollah-zadeh, M. Asgari, M. A. Ghaffari, Influence of Si content on the wettability and corrosion resistance of nanocomposite TiSiN films deposited by pulsed-DC PACVD, *Journal of Alloys and Compounds* 739, 780–792 (2018); doi: 10.1016/j.jallcom.2017.12.235.
5. A. Niederhofer, T. Bolom, P. Nesladek, K. Moto, C. Eggs, D. Patil, S. Vepřek, The role of percolation threshold for the control of the hardness and thermal stability of super- and ultrahard nanocomposites, *Surface and Coatings Technology* 146-147, 183–188 (2001); doi: 10.1016/S0257-8972(01)01469-4.
6. W. Gissler, Structure and properties of Ti-B-N Coatings, *Surface and Coatings Technology*, 556–563 (1994).

7. K. H. Kim, J. T. Ok, S. Abraham, Y.-R. Cho, I.-W. Park, J. J. Moore, Syntheses and mechanical properties of Ti–B–C–N coatings by a plasma-enhanced chemical vapor deposition, *Surface and Coatings Technology* 201, 4185–4189 (2006); doi: 10.1016/j.surfcoat.2006.08.051.
8. P. H. Mayrhofer, C. Mitterer, J. E. Greene, Thermally induced self-hardening of nanocrystalline Ti-B-N thin films, *Journal of Applied Physics* (2006).
9. H. Paschke, M. Stueber, C. Ziebert, M. Bistron, P. Mayrhofer, Composition, microstructure and mechanical properties of boron containing multilayer coatings for hot forming tools, *Surface and Coatings Technology* 205, 24-28 (2011); doi: 10.1016/j.surfcoat.2011.04.097.
10. P. Mahato, G. Nyati, R. J. Singh, S. K. Mishra, Nanocomposite TiSiBC Hard Coatings with High Resistance to Wear, Fracture and Scratching, *Journal of Materials Engineering and Performance* 25, 3774–3782 (2016); doi: 10.1007/s11665-016-2239-5.
11. P. Mahato, R. J. Singh, S. K. Mishra, Nanocomposite Ti–Si–B–C hard coatings deposited by magnetron sputtering: Oxidation and mechanical behaviour with temperature and duration of oxidation, *Surface & Coatings Technology*, 230–240 (2016).
12. P. Mahato, S. K. Mishra, M. Murmu, N. C. Murmu, H. Hirani, P. Banerjee, A prolonged exposure of Ti-Si-B-C nanocomposite coating in 3.5 wt% NaCl solution: Electrochemical and morphological analysis, *Surface and Coatings Technology* 375, 477–488 (2019); doi: 10.1016/j.surfcoat.2019.07.039.
13. D. Verma, D. Banerjee, S. K. Mishra, Effect of Silicon Content on the Microstructure and Mechanical Properties of Ti-Si-B-C Nanocomposite Hard Coatings, *Metallurgical and Materials Transactions A* 50, 894–904 (2019); doi: 10.1007/s11661-018-5028-y.
14. P. Mahato, S. K. Mishra, N. C. Murmu, P. Banerjee, Enhancement of the Mechanical and Tribological Performance of Stainless Steel 304 by Ti-based Nanocomposite Coatings Deposited by PVD Method, *Triboindia* (2018).
15. P. Mahato, P. Banerjee, M. Murmu, H. Hirani, N. C. Murmu, S. K. Mishra, Investigation on Multifunctional Properties of Sputtered Ti-Si-B-C Coating with Varied Thickness over Targeted Surface, *Journal of Materials Engineering and Performance* 30, 4432–4444 (2021); doi: 10.1007/s11665-021-05633-3.
16. S. K. Mishra, P. Mahato, B. Mahato, L. C. Pathak, Thermal stability and effect of substrate temperature of TiSiBC hard nanocomposite coatings on microstructure, mechanical, thermal behaviour deposited by magnetron sputtering, *Applied Surface Science* 266, 209–213 (2013); doi: 10.1016/j.apsusc.2012.11.149.
17. S. K. Mishra, A. S. Bhattacharyya, P. Mahato, L. C. Pathak, Multicomponent TiSiBC superhard and tough composite coatings by magnetron sputtering, *Surface and Coatings Technology* 207, 19–23 (2012); doi: 10.1016/j.surfcoat.2012.03.047.
18. A. Thewes, L. Bröcker, E. T. K. George, G. Bräuer, M. Paulus, C. Sternemann, H. Paschke, T. Brückner, S. Lechner, S. Müller, Ti-Si-B-C-N plasma enhanced chemical vapor deposition nanocomposite coatings for high temperature applications, *Thin Solid Films* 760, 139507 (2022); doi: 10.1016/j.tsf.2022.139507.
19. S. Zak, C. O. W. Trost, P. Kreiml, M. J. Cordill, Accurate measurement of thin film mechanical properties using nanoindentation, *Journal of Materials Research* 37, 1373–1389 (2022); doi: 10.1557/s43578-022-00541-1.
20. C. Krywka, M. Paulus, C. Sternemann, M. Volmer, A. Remhof, G. Nowak, A. Nefedov, B. Pöter, M. Spiegel, M. Tolan, The new diffractometer for surface X-ray diffraction at beamline BL9 of DELTA, *Journal of synchrotron radiation* 13, 8–13 (2006); doi: 10.1107/S0909049505035685.
21. M. Abedi, A. Abdollah-zadeh, M. Bestetti, A. Vicenzo, A. Serafini, F. Movassagh-Alanagh, The effects of phase transformation on the structure and mechanical properties of TiSiCN nanocomposite coatings deposited by PECVD method, *Applied Surface Science* 444, 377–386 (2018); doi: 10.1016/j.apsusc.2018.02.263.
22. P.-C. Tsai, W.-J. Chen, J.-H. Chen, C.-L. Chang, Deposition and characterization of TiBCN films by cathodic arc plasma evaporation, *Thin Solid Films* 517, 5044–5049 (2009); doi: 10.1016/j.tsf.2009.03.029.

Proceedings of the SICT 2024 International Conference
Vienna, Austria – April 17 – 19, 2024
DOI: https://doi.org/10.26799/cp-sict-2024

Influence of current density and process time on structural, chemical and physical behavior of anodized aluminum

Breu Lea[1,2], Bubrin Martina[1], Sörgel Timo[2]
[1]Robert Bosch Manufacturing Solutions GmbH
Wernerstr. 51, Stuttgart, Germany, Lea.Breu@de.bosch.com
[2]Center for Electrochemical Surface Technology ZEO, Aalen University of Applied Sciences
Beethovenstr. 1, Aalen, Germany

Abstract

Anodization of aluminum is a useful process to improve the corrosion resistance of aluminum. For industrial application, the required process time is an important parameter due to its direct influence on production costs. However, when speeding up the process, layer properties must not be altered. In this study porous aluminia layers are produced on 6061 aluminum alloy substrates from an oxalic acid electrolyte to investigate the impact of current density and process time on microstructure and corrosion resistance. Especially the high current density end is investigated in greater detail. To determine corrosions resistance and microstructure of the layer, electrochemical impedance spectroscopy (EIS) and scanning electron microscopy (SEM) are used, respectively. As a result, similar structures and corrosion resistances can be obtained throughout a wide range of current densities. The layers exhibit an uncommon coral-like microstructure with interrupted pores and frayed walls. At the upper end of the investigated current density range, tubular aspects of the structure become more dominant, while the surface shows a higher degree of redissolution and corrosion resistance decreases.

Keywords: Anodizing, oxalic acid, high current density, corrosion resistance, electrochemical impedance spectroscopy

1. Introduction

In upcoming technologies hydrogen plays an important role, for examples in fuel cells, electrolyzers, in mobility sector and for energy storage. Hydrogen handling sets new requirements on the used materials. It thereby comes into contact with, often demanding hydrogen barrier layers the protect the substrate material itself from hydrogen embrittlement. An alternative to high strength steel materials is the use of suitable aluminum alloys [1]. Yet the latter is vulnerable to corrosion and wear due to environmental influences and depending on the specific application requirements. To avoid corrosion, aluminum generally is anodized. To date, several studies have confirmed the effectiveness of anodizing to improve the corrosion resistance [2]–[5]. A prior study has noted that corrosion resistance of AA6061 is not increased with higher current densities while anodizing with sulfuric acid [4]. Cabral-Miramontes et al. have shown that the use of citric acid electrolytes can improve corrosion resistance with higher current densities compare to sulfuric acid electrolyte [3], using etidronic acid can also improve the corrosion resistance and accelerate the process [5]. However, according to Mohammadi and Afshar, microstructure can influence corrosion resistance and generally the thicker the barrier layer the better [6]. Yet imperfections of the anodized layer on AA 6061 alloy, frequently occurring with longer process times can be detrimental, so thicker layers are not generally better [7]. Also bigger pore diameter, higher layer porosity and irregular pore structure decrease corrosion resistance when anodizing in sulfuric acid [8]. Other studies have shown that oxalic acid is the preferred electrolyte for anodizing AA6061 in order to achieve improved corrosion resistance when compared to sulfuric acid [9], [10].

2. Material and Methods

Disk shaped substrates from a commercial 6061 aluminum alloy with a diameter of 24 mm and a thickness of 8 mm were used.

2.1. Anodizing

Before anodizing the raw material was pretreated. First it was degreased in a commercial degreasing solution (New Dimensions Supreme, MacDermid Enthone) for 5 min at 60 °C. After that it was pickled in a commercial pickling solution (Alumon AC 10, Alumon AC 70, MacDermid Enthone) for 2 min at room temperature. As a last pretreatment step, pickling residues are removed with a commercial solution (Alumon AC 10, Alumon MS, MacDermid Enthone) for 30 s at room temperature. Between each step, the sample was rinsed in deionized water. For the anodizing step, a 2.5 wt% oxalic acid (Merck KGaA) electrolyte. The electrolyte temperature was kept constant at 20 °C within a range of +/- 2 °C and was cooled with a recirculation chiller (F4006 –

DOI: https://doi.org/10.26799/cp-sict-2024

Julabo, Seelbach, Germany). The anodizing was performed in a 160 L cell bath with more than 40 times larger stainless steel electrodes than the samples. As current source, a rectifier was used (VE3PUI2 150.30 - Kniel, Karlsruhe, Germany). The process was current controlled with different current densities between 0.5 and 15 A/dm². To assure comparability, every layer should have an equal layer thickness of 6 µm +/- 1 µm. Therefore, each anodization experiment was performed with the same electrical charge which automatically converts to different process times. Table 1 shows the various process parameters. After anodizing, as a last process step, the component was leached in deionized water for 5 min at room temperature.

Table 1: process parameter.

current density [A/dm²]	0.5	1	5	15
process time [s]	3000	1500	300	100

2.2. Characterization

SEM micrographs were used to characterize the microstructure of the layers. Therefore, pictures of the surface and the cross section were taken. For quantitative analysis the software package fjii ImageJ 1.54f (U. S. National Institutes of Health, Bethesda, Maryland, USA) was used. Each value is the result of ten measurements.

Corrosion resistance was analysed with Electrochemical Impedance Spectroscopy (EIS) and potentiodynamic polarisation tests. Therefor a potentiostat (VSP – BioLogic, Seyssinet-Pariset, France) was used. A three-electrode cell (FlexCell – Gaskatel Gesellschaft für Gassysteme durch Katalyse und Elektrochemie mbH, Kassel, Germany) configuration was used, with the aluminium component as a working electrode, platin wire as a counter electrode and a standard H_2-electrode (Mini-HydroFlex – Gaskatel Gesellschaft für Gassysteme durch Katalyse und Elektrochemie mbH, Kassel, Germany) as references electrode. Experiments were performed in a 3.5 wt.% NaCl electrolyte. Initially, each sample was immersed in the electrolyte for 12 h. After that, the impedance was measured in frequency range of 200 kOhm to 10 mOhm with an amplitude of 10 mV. The polarisation test was performed +/- 250 mV against open circuit voltage with a potential sweep rate of 1 $mV*s^{-1}$.

3. Results

3.1. Microstructure

Barrier layer and pore diameter were analysed on the surface and in cross section. With increasing current densities, required process voltages also increase. As a result, also the barrier layer thickness increases proportionally to the voltage [11]. Fig. 1 shows, that the barrier layer has homogenies thickness and grows with higher current densities. The 5 and 15 A/dm² samples have the same maximal process voltage, but the 5 A/dm² layer has the thicker barrier layer. So there is a maximum in barrier layer thickness.

DOI: https://doi.org/10.26799/cp-sict-2024

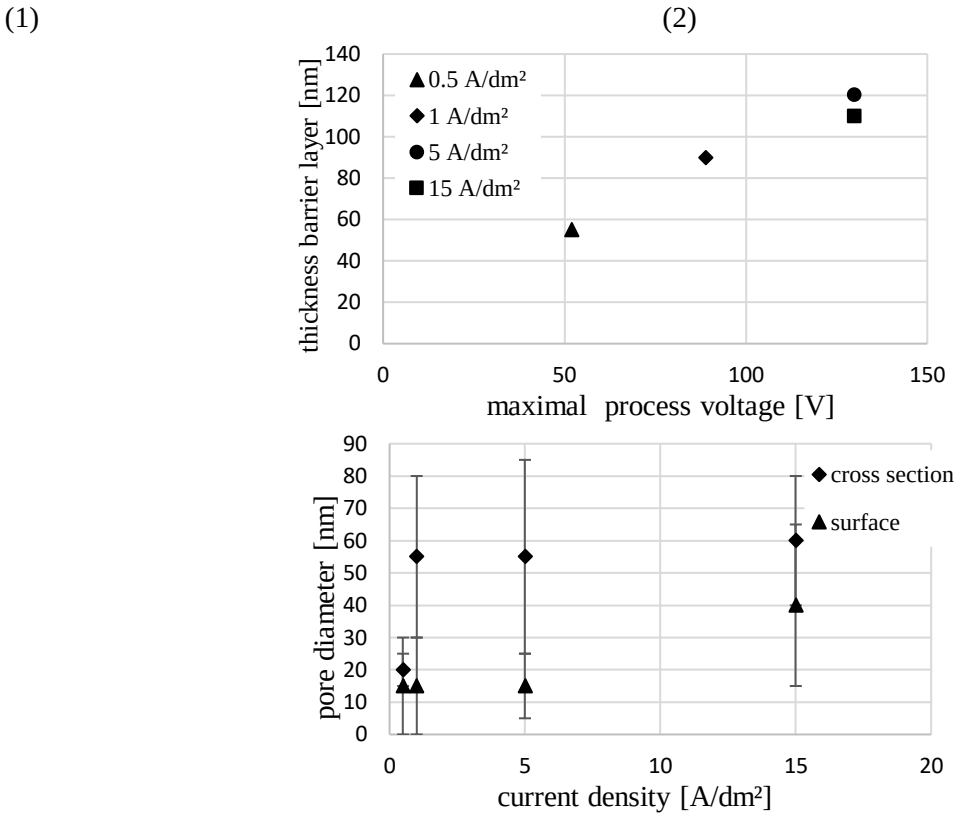

Fig. 1: Characterisation microstructure of anodizing layers: (1) thickness barrier layer (2) pore diameter

For each layer, the pore diameters, evaluated by top view and cross section are different (fig. 1), with the exception for the layer formed at 0.5 A/dm² layer, where the pore diameter is small and similar on the surface and in cross section. The fluctuations in the measurements are small, which shows that the pores are uniform and homogeneous in pore diameters. At average current density, pore diameters evaluated from top view and cross section differ more widely, also there are large fluctuations in the respective measured values. But there is a clear trend towards larger pore diameters in the cross section. In cross section the pores are less uniform and have a wide range of pore diameters in a single layer. The pore diameter differs by 30 nm between surface and cross section at 1 and 5 A/dm², respectively. It is as if the pores are growing together as they approach the surface. The pores on the surface become larger and fewer as current density and voltage increases (fig. 2). At 15 A/dm², the SEM pictures clearly show chemical dissolution on the surface. In picture (4) top (fig. 2) it can be seen that pore walls on the surface have been dissolved. The pores bond with each other. The larger pore diameter on surface can be explained by this.

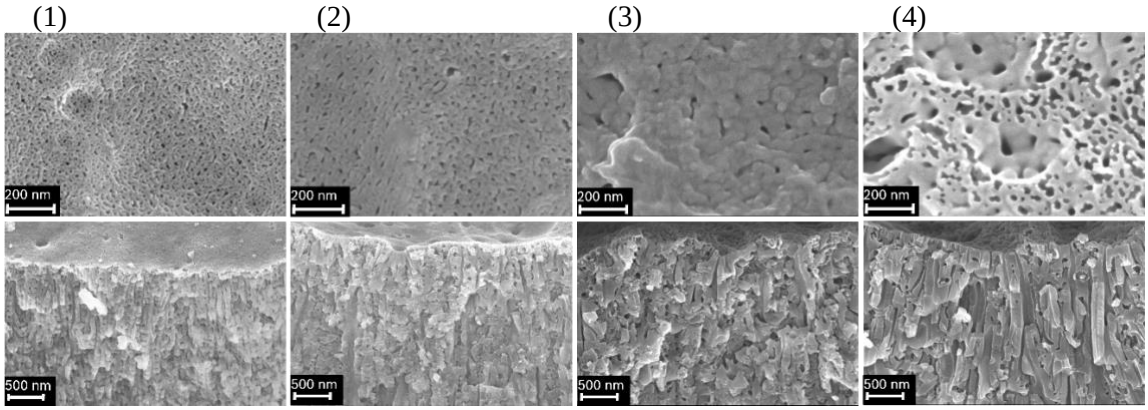

Fig. 2: SEM mircographs of surface (top) and cross section (bottom) from (1) 0.5 A/dm² (2) 1 A/dm² (3) 5 A/dm² and (4) 15 A/dm²

In cross section, the microstructure of the layers are clearly shown, but different as expected from literature. The typical microstructure of an anodized layer, generally shows uniform and equal pores in terms of pore

DOI: https://doi.org/10.26799/cp-sict-2024

diameter, straightness and orientation [12]. Here, the layers don´t show straight and oriented pores, the structure can be explained as coral-like (fig. 2). The pores aren´t continuous and perpendicularly aligned next to each other. Additionally, the pore walls are frayed. This kind of structure can be seen at 0.5, 1 and 5 A/dm². At 15 A/dm², the pores are more tubular.

3.2. Corrosion resistance

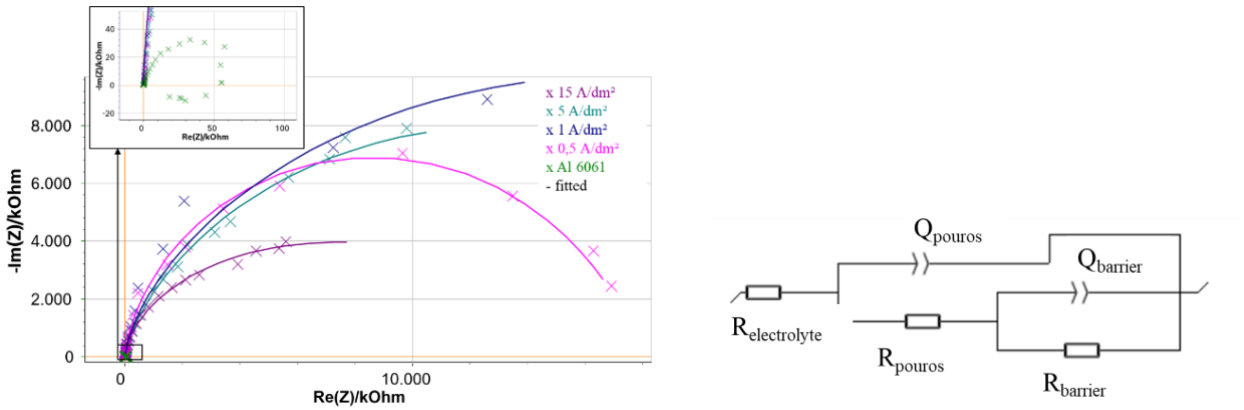

Fig. 3: Electrochemical impedance spectroscopy measurements and the equivalent electric circuit used for fitting

EIS measurments confirm an improved corrosion protection in comparison with the untreated substrate for any type of anodizes layer formed (fig. 3). Layer formed at 1 and 5 A/dm² exhibit the best corrosion resistance, which is quite similar in both cases. 15 A/dm² with the shortest process time, but one of the thickest barrier layers improves the corrosion resistance as least. This shows, that the barrier layer thickness isn´t the only property of the layer, related to corrosions resistance. Furthermore, the chemical re-dissolution of alumina, which continuously happens while in contact with the oxalic acid electrolyte, decreases the corrosion resistance, as this process leads to an increased layer porosity. Table 2 shows the various corrosion rates, calculated from polarisation tests. There is a significant drop from 1500 nm per year (nm/year) for the untreated substrate to 4 nm/year for the layers formed at 0.5 A/dm² and 5 A/dm². This similarity is unexpected, as the barrier layer of the layer formed at 5 A/dm² is twice as thick. So again, this also underlines the previous statement. In summary, this finding is contrary to previous studies which have suggested that thicker barrier layers increase and non-tubular pores decrease corrosion resistance [6], [8].

Table 2: corrosion rate

current density [A/dm²]	uncoated	0.5	1	5	15
corrosion rate [nm/year]	1500	4	-*	4	18

* not possible to evaluate

4. Conclusion

The anodized layers investigated here show an uncommon structure, which can described as coral-like. It is shown that deposition times can be shortened without in every case sacrificing the degree of corrosion protection. This is an important issue for future research about economic optimization through process time reduction.
It is shown, that in the investigated system, corrosion resistance is not solely determined by barrier layer thickness. Also the microstructure, resulting from deposition parameters and chemical re-dissolution processes, plays an important role. Future work should focus on the quantitative determination of the parameter-property relationships in the system.

Acknowledgements

The author thanks Michael Kaupp for his support creating the measurement program and the exchange during the corrosion measurements and Dr. Wassima El Mofid for introduction into the EIS measurements.

DOI: https://doi.org/10.26799/cp-sict-2024

References

1. "Addendum 13: UN Global Technical Regulation No. 13 Hydrogen and Fuel Cell Vehicles," Global Technical Regulations 13, Jun. 2023. Accessed: May 10, 2024. [Online]. Available: https://unece.org/transport/standards/transport/vehicle-regulations-wp29/global-technical-regulations-gtrs
2. S.-J. Lee and S.-J. Kim, "Essential anti-corrosive behavior of anodized Al alloy by applied current density," *Appl. Surf. Sci.*, vol. 481, pp. 637–641, Jul. 2019, doi: 10.1016/j.apsusc.2019.03.155.
3. J. Cabral-Miramontes *et al.*, "Citric Acid as an Alternative to Sulfuric Acid for the Hard-Anodizing of AA6061," *Metals*, vol. 11, no. 11, p. 1838, Nov. 2021, doi: 10.3390/met11111838.
4. I. C. Chung, C. K. Chung, and Y. K. Su, "Effect of current density and concentration on microstructure and corrosion behavior of 6061 Al alloy in sulfuric acid," *Surf. Coat. Technol.*, vol. 313, pp. 299–306, Mar. 2017, doi: 10.1016/j.surfcoat.2017.01.114.
5. H. Huang *et al.*, "Ultra-fast fabrication of porous alumina film with excellent wear and corrosion resistance via hard anodizing in etidronic acid," *Surf. Coat. Technol.*, vol. 393, p. 125767, Jul. 2020, doi: 10.1016/j.surfcoat.2020.125767.
6. I. Mohammadi and A. Afshar, "Modification of nanostructured anodized aluminum coatings by pulse current mode," *Surf. Coat. Technol.*, vol. 278, pp. 48–55, Sep. 2015, doi: 10.1016/j.surfcoat.2015.08.004.
7. S. H. Mohitfar, M. R. Etminanfar, S. Mahdavi, and J. Khalil-Allafi, "Characteristics and corrosion resistance of hard-anodised 6061-T6 aluminium alloy," *Trans. IMF*, vol. 101, no. 4, pp. 196–204, Jul. 2023, doi: 10.1080/00202967.2023.2208438.
8. P. Zhang and Y. Zuo, "Effects of pore parameters on performance of anodic film on 2024 aluminum alloy," *Mater. Chem. Phys.*, vol. 231, pp. 9–20, Jun. 2019, doi: 10.1016/j.matchemphys.2019.04.008.
9. Y. Huang *et al.*, "Evaluation of the corrosion resistance of anodized aluminum 6061 using electrochemical impedance spectroscopy (EIS)," *Corros. Sci.*, vol. 50, no. 12, pp. 3569–3575, Dec. 2008, doi: 10.1016/j.corsci.2008.09.008.
10. M. Franco, T. Hari Krishna, A. M. Pillai, A. Rajendra, and A. K. Sharma, "A comparative study on the corrosion behaviour of hard anodic coatings on AA 6061 obtained using DC and pulsed DC power sources," *Acta Metall. Sin. Engl. Lett.*, vol. 26, no. 6, pp. 647–656, Dec. 2013, doi: 10.1007/s40195-013-0091-2.
11. J. Li *et al.*, "Self-Organization Process of Aluminum Oxide during Hard Anodization," *Electrochimica Acta*, vol. 213, pp. 14–20, Sep. 2016, doi: 10.1016/j.electacta.2016.06.044.
12. F. Keller, M. S. Hunter, and D. L. Robinson, "Structural Features of Oxide Coatings on Aluminum," *J. Electrochem. Soc.*, vol. 100, no. 9, p. 411, 1953, doi: 10.1149/1.2781142.

Proceedings of the SICT 2024 International Conference
Vienna, Austria – April 17 – 19, 2024
DOI: https://doi.org/10.26799/cp-sict-2024

The impact of growth conditions on the crystalline quality and surface morphology of epitaxial III-N thin film: A molecular dynamics simulation

Zaiter Ayla[1], Clavier Germain[1], Hounkpati Viwanou[1], Chen Jun[1]
[1] Normandie Univ, ENSICAEN, UNICAEN, CEA, CNRS, CIMAP, 14000 Caen, France
ayla.zaiter@unicaen.fr

Abstract

The high quality GaN thin films is of great significance for increasing the lifetime and performance of GaN device. By using the molecular dynamics (MD) with an empirical Stillinger-Weber potential, we studied the impact of various growth conditions on the crystalline quality of GaN films at the atomic scale, such as temperature and growth rate. The analysis focuses on the crystal structure and the surface morphology of films deposited under varying growth conditions.

Keywords: GaN, Molecular dynamics, Stillinger-Weber, Growth condition

1. Introduction

Semiconductor III-N such as indium nitride (InN), gallium nitride (GaN) and aluminium nitride (AlN) are widely used in optoelectronic and electronic devices such as light-emitting diodes (LEDs), laser diodes (LDs), ultraviolet (UV) detectors and more [2]. This is due to their thermal and chemical stability, allowing them to withstand challenging operating conditions, including high temperatures, high voltages, and currents. They also possess a wide direct bandgap of 0.7 eV, 3.3 eV and 6.2 eV, respectively [1]. Alloys like AlGaN, InGaN, and AlInN cover the spectrum from visible to near-infrared (IR) wavelengths, making III-N materials attractive for optoelectronic devices in the green, blue, and UV spectral range.

The III-N materials are most commonly employed in the form of thin layers obtained through epitaxial growth on substrates made of other materials. Though, the growth of the high quality III-N epilayers is influenced by the growth conditions such as temperature, growth rate and incident energies.

In this study, the deposition process of an GaN on a GaN substrate is simulated using the molecular dynamic. The effect of growth temperature and injected N/Ga flux ratio on the surface morphology, and atomic structure of GaN deposited film are considered.

2. Calculation Methods

2.1. Interatomic potential

The accuracy of MD simulation depends on the potential energy function used to describe particle interactions. In this work, the Stilling-Weber InGaN interaction potential is used to describe the atomic interactions in GaN systems [2]. The related parameters are given in Table 1.

Table 1: Parameters of the Stilling-Weber potential for InGaN [2].

Pair ij	ε	σ	a	A	B
GaGa	2.926	1.759	1.604	7.917	0.955
NN	4.420	1.726	1.630	7.917	0.969
GaN	2.289	1.715	1.799	7.917	0.641

Molecular dynamics simulation was performed using the Large-scale Atomic/Molecular Massively Parallel Simulator (LAMMPS) code [3] to simulate the growth process of the GaN film on the GaN substrate.

2.2. Simulation Details

The deposition model of the GaN film on the GaN substrate is shown in Fig.1. The GaN substrate consists of 11088 atoms (5544 Ga atoms and 5544 N atoms) with Ga terminated surface. The growth direction of the substrate is along the polar direction [0001] and aligned with Z direction in our simulation. The substrate was divided into three parts. The two layers of atoms at the bottom of the substrate were fixed to prevent the full GaN substrate from moving during deposition. The two layers at the top of the substrate constituted the free group, where the atoms could interact freely with deposited atoms. In this region, the

DOI: https://doi.org/10.26799/cp-sict-2024

equations of motion were integrated using a standard velocity verlet algorithm. The atoms in the middle region were coupled to a Nosé-Hoover chain thermostat to control the system temperature. Periodic boundary conditions are applied to the direction of x and y, the free boundary condition is applied in z direction to enable the deposition of Ga and N atoms towards the substrate surface. The growth of GaN film is simulated by injecting Ga and N atoms vertically (incident angle $\theta = 0°$) from 90 Å towards the substrate. The kinetic energy of the injected atoms was set to 0.1eV. The number of injected Ga atoms is 8000, while the injected N atoms is defined by N/Ga flux ratio which is set as a simulation parameter.

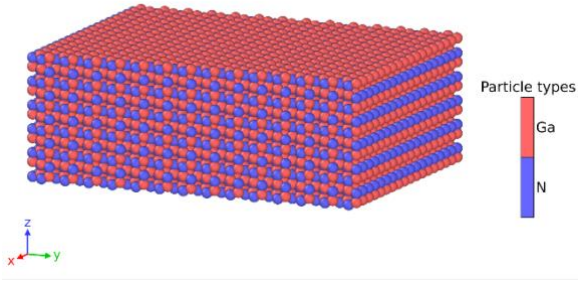

Fig. 1: 3D model of GaN substrate.

2.3. Analysis Methods

The visualisation of GaN substrate and deposited GaN film is done using the open visualization tool (OVITO) [6]. Atoms organized in a hexagonal (wurtzite) or cubic diamond (zinc blende) lattice can be identified using diamond structure (IDS) tool. The second nearest neighbours are taken into account to distinguish the two structures wurtzite and zinc blende structures. The surface roughness of deposited GaN film under different conditions is represented by the root-mean-square (RMS) roughness R_a:

$$\mathrm{R}_a = \sqrt{\frac{\sum_1^N (Z_i - \bar{Z})^2}{N}} \quad (1)$$

In this equation, Z_i represents the z coordinate of the surface atom i, $\bar{Z}$ represents the average z coordinate of all the surface atoms, and N denotes the total number of surfaces atoms of the deposited GaN film.

3. Results and discussion

3.1. Effect of deposition rate

A smooth surface is a critical indicator of high quality GaN film. Numerical simulations are performed in order to examine the impact of deposition rate on the crystallinity of the deposited layer. To compare with experimental results, we'll express the simulation temperature in reduced temperature $T^* = T/T_m$ where T_m is the melting temperature of the model. The computed value of T_m =$3570K$, higher than the experimental value (T_m =$2493K$)[4]. Three deposition rates are chosen, each with a N/Ga ratio of 1 and a temperature of $T^* = T/T_m$=0.50 with 1 atom/1 ps, which is equivalent to 0.005Å/ps, 1 atom/3 ps, which is equivalent to 0.002Å/ps, and 1 atom/5 ps, which is equivalent to 0.001 Å/ps. For these various rates of 1 atom/1 ps, 1 atom/3 ps, and 1 atom/5 ps, the deposition procedure takes 8000 ps, 24000 ps, and 40000 ps, respectively. Following deposition, the system is brought into equilibrium by a 6000 ps relaxation process.

We observe a significant improvement in crystallinity, increasing from 70% for a deposition rate of 1 atom/1 ps to 79% for a rate of 1 atom/3 ps. This enhancement can be explained by the fact that deposited atoms have a greater probability of finding an ideal lattice site before being affected by the arrival of other atoms.

The influence of the growth rate on the properties of GaN films has been experimentally studied by Shuti [5]. They observed that the properties of GaN film are improved when the deposition rate is properly controlled. However, the quality of the GaN film deteriorates when the growth rate decreases. The simulations reported above are clearly consistent with the experimental findings.

3.2. Effect of temperature

In order to study the influence of temperature on the surface morphology and crystallinity of the deposition GaN film, the surface morphology of the deposited GaN films grown on GaN substrates after relaxation is

DOI: https://doi.org/10.26799/cp-sict-2024

shown in Fig3. Fig 3 shows the surface morphology of the deposited GaN film under different temperatures T^*=0.31, T^*=0.50 and T^*=0.70. From this figure, we find the surface gets smoother when the temperature increases and the growth mode changed to layered growth (2D). Using equation 1, the surface roughness of GaN during deposition and structure component are calculated, as shown in Fig 4. An increase in surface roughness is observed with deposition time for a temperature T^*=0.31. The roughness decreases for a temperature T^*=0.70 and the crystallinity increases.

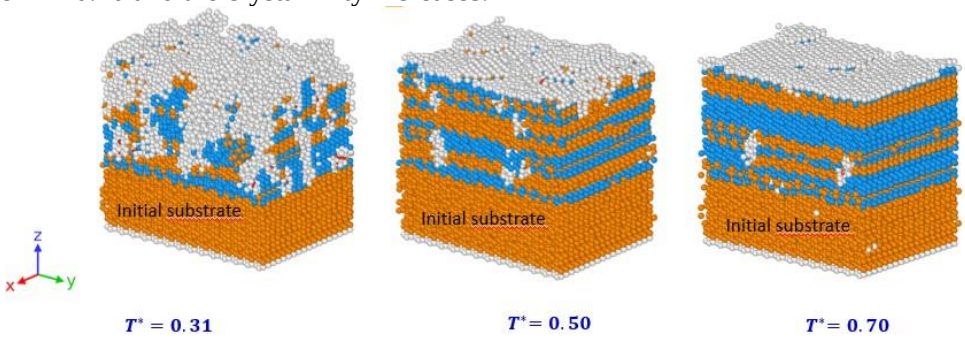

Fig. 3: Atomic structure distributions of the deposited GaN films at different growth temperatures.

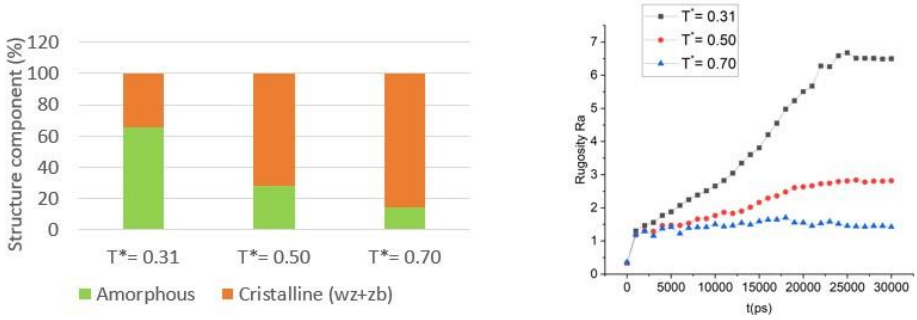

Fig. 4: Structure component and roughness of GaN film during deposition under different temperature.

3.3. Effect of ratio N/Ga

In this section, we investigate the influence of the N/Ga ratio on the crystallinity and surface morphology of the deposition layer. To explore these aspects, numerical simulations are conducted using a deposition rate of 1 atom/3ps, while maintaining the temperature constant T^*=0.50. These simulations are performed for various N/Ga, namely 0.8,1,1.2 and 1.4. Figure 5 show the percentage of crystalline structure of deposited GaN under different injected N/Ga ratios. The figure shows that we have a better crystallinity for N/Ga ratio of 1, with a degree of crystallinity of 89%. By increasing this ratio from 1.2 to 1.4, the crystallinity decreases from 74% to 59% accompanied by an increase in the percentage of the amorphous structure from 26% to 41%. For low N contents, the Ga adatoms with high surface mobility dominate the growth mechanisms, leading to a good cristallinity, has also been proven by experiment [5]. To explain this behavior, we calculate the diffusion activation energy barriers for a nitrogen and a gallium atom on an Ga-terminated (0001) surface. We found 1.3 eV and 0.7eV respectively by using the potential, compared to 1.1–1.3 eV and 0.2–0.7 eV, for a nitrogen and gallium atoms respectively on a Ga-terminated (0001) surface based on ab initio calculations.

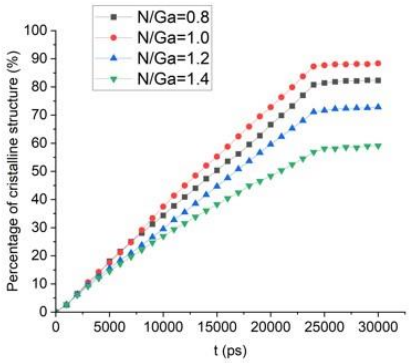

Fig. 5: Percentage of crystalline structure of deposited GaN under different injected N/Ga ratios

DOI: https://doi.org/10.26799/cp-sict-2024

4. Conclusion

This work used MD modeling to examine the formation of GaN film on GaN substrate. The deposition rate, growth temperature, and injected N: Ga flux ratio were examined. It was discovered that high growth temperature effectively improved the surface morphology and crystallinity of deposited GaN films due to enhanced adatom mobility. Additionally, when the injected N: Ga flux ratio is near to 1.0, excellent morphology and crystallinity of the GaN layer can be attained. These findings the importance of controlled growth conditions in obtaining high-quality GaN films.

Acknowledgements

The authors thank CRIANN (https://www.criann.fr/) where computations were performed using HPC resources.

References

1. O. Ambacher, "Growth and applications of group iii-nitrides," Journal of Physics D: Applied Physics, vol. 31, pp. 2653 – 2710, 1998. X. W. Zhou and R. E. Jones, "A Stillinger-weber potential for InGaN," Journal of Materials Science Research, vol. 6, p. 88, 2017.
2. S. Plimpton, "Fast parallel algorithms for short-range molecular dynamics," Journal of Computational Physics, vol. 117, no. 1, pp. 1–19, 1995.
3. X.W. Zhou, R.E. Jones, J. Gruber, "Molecular dynamics simulations of substitutional diffusion," Journal of Materials Science Research, vol. 128, p. 331-336, 2017.
4. S. Li, J. Su, G. Fan, Y. Zhang, S. Zheng, H. Sun, and J. Cao, "Influence of growth rate in the early stage of high temperature GaN layer growth on quality of GaN films," Journal of Crystal Growth, vol. 310, no. 16, pp. 3722–3725, 2008.
5. J.-K. Tsai, I. Lo, K.-L. Chuang, L.-W. Tu, J.-H. Huang, C.-H. Hsieh, and K.-Y. Hsieh, "Effect of N to Ga flux ratio on the GaN surface morphologies grown at high temperature by plasma-assisted molecular-beam epitaxy," Journal of Applied Physics, vol. 95, pp. 460–465, 01 2004.
6. A. Stukowski, "Visualization and analysis of atomistic simulation data with ovito–the open visualization tool," Modelling and Simulation in Materials Science and Engineering, vol. 18, p. 015012, dec 2009.

Proceedings of the SICT 2024 International Conference
Vienna, Austria – April 17 – 19, 2024
DOI: https://doi.org/10.26799/cp-sict-2024

Reactive sputtering of ceramic hydrogen barrier coatings

Anne Zirbel[1,2], Lea Haus[1], Simon Hübner[4], Matthias Müller[1], Jens Riedel[3], Sven Ulrich[2]
[1]Robert Bosch Manufacturing Solutions GmbH
Wernerstraße 51, 70469 Stuttgart, Germany, anne.zirbel@de.bosch.com
[2]Karlsruher Institute of Technology, Institute for Applied Materials
Hermann-von-Helmholtz-Platz 1, 76344 Eggenstein-Leopoldshafen Germany, sven.ulrich@kit.edu
[3]iChem Analytics GmbH
Bad Meinberger Straße 1, 32760 Detmold, Germany, jens.riedel@ichemanalytics.de
[4]Singulus Technologies AG
Hanauer Landstraße 103, 63796 Kahl am Main, Germany, simon.huebner@singulus.de

Abstract

Hydrogen plays a major role as a future energy source. Its properties and interactions with metals lead to material science challenges. In order to reduce the risk of hydrogen embrittlement, hydrogen barrier coatings are being developed in this work. Due to the high layer quality of PVD layers, all considered layers are produced by sputtering. The focus was on the coating systems zirconium nitride, diamond like carbon (DLC) and tungsten carbide. To evaluate the barrier effect, hydrogen permeation measurements were carried out with an electrochemical and a gas-driven method and their comparability was checked. In particular, tungsten carbide was able to convince with an outstanding barrier effect and a permeation reduction factor (PRF) in the range of 10^5.

Keywords: hydrogen permeation barrier coating, reactive magnetron sputtering, tungsten carbide, zirconium nitride, permeation reduction factor

1. Introduction

In the course of the energy transition and the establishment of renewable energies, hydrogen as an energy carrier plays an important role both as a fuel in direct combustion and in energy conversion in fuel cells and electrolysers. However, new challenges arise from its properties. As the smallest and lightest element, hydrogen requires only a very low activation energy for diffusion in solids, even at low temperatures. The diffusion of hydrogen in iron at room temperature is about 10 to 15 orders of magnitude higher than the diffusion of carbon, nitrogen or oxygen. The high mobility and interaction of the penetrating hydrogen with the lattice of some metals results in a high risk of hydrogen embrittlement. Affected components should therefore be protected by a hydrogen permeation barrier layer. Important for the effectiveness of such a barrier layer is a high layer quality, hence methods of physical vapor deposition (PVD) are particularly suitable.

2. Materials and methods

2.1. Coating deposition

All coatings were deposited by magnetron sputtering. Two different system types were used, firstly a batch production line of the type PCS1000 from Robert Bosch Manufacturing Solutions GmbH and secondly an inline coating line of the type Vistaris 600 from Singulus Technologies AG. The layers were applied to a ferritic steel (1.4016). The coating systems zirconium nitride [5,6], diamond like carbon (DLC) and tungsten carbide [1,4] were considered. In the systems zirconium nitride and tungsten carbide, process parameters and layer thickness were varied in order to determine their influence on the barrier effect.

2.2. Hydrogen permeation measurement methods

Two hydrogen permeation measurement methods were used to evaluate the hydrogen barrier effect. The electrochemical variant used is a further development of the classic Devanathan-Stachurski method. The sample to be examined separates the loading side from the measuring side. The functional principle of the electrochemical double cell is similar to a fuel cell. The loading side is filled with an electrolyte, here 0.5mol sodium hydrogen carbonate ($NaHCO_3$), which serves as a hydrogen supplier. An oxygen electrode is installed on the measuring side, which is the driving force for the oxidation of the hydrogen diffused through the sample [3]. Using the recorded hydrogen oxidation current, the amount of charge exchange can be determined as a characteristic value. This value serves as a comparison and evaluation parameter for the electrochemical analysis, which is mainly performed at room temperature.

DOI: https://doi.org/10.26799/cp-sict-2024

The second variant is a gas-driven method that separates two vacuum chambers from each other. On the loading side, hydrogen will be admitted as a gas. A mass spectrometer is used on the measuring side for time-resolved gas analysis. Using an integrated heating system, test temperatures of up to 250°C can be achieved. The signal of the mass spectrometer makes it possible to determine the diffusion coefficient at a selected temperature as well as the permeation reduction factor of a coating system. The permeation reduction factor (PRF) is described by the ratio of the steady-state ion currents of an uncoated substrate, $j_{uncoated}$, compared to a coated sample, j_{coated}, and is therefore often used as an evaluation criterion for the barrier effect of a coating [2,7]. The larger the PRF, the better the barrier effect.

3. Results

Zirconium nitride was extensively investigated with the electrochemical permeation measurement. The influence of process parameters such as coating temperature and nitrogen flow as well as the influence of the layer thickness on the permeation behavior were investigated. A ZrN-coated sample shows a significantly reduced permeation compared to the uncoated reference. An increase in coating temperature showed no effect on the barrier effect, while an increased nitrogen input (125 sccm vs 100 sccm) resulted in a significant deterioration of about 30% with an amount of charge exchanged of 3.5 mAs instead of 2.7 mAs within 2h. The goal of occupying all interstitial lattice sites in the Zr lattice with nitrogen and thereby achieving a high barrier effect was not achieved. Most likely, the increased nitrogen incorporation led to large lattice distortions, which create new spaces and thus promote diffusion. The coating thickness variation provided very interesting results. The ZrN layer with a low layer thickness of only 200 nm formed a significantly weaker barrier (2.7 mAs) than the layers with a thickness of 500nm (1.7 mAs). A further increase of the layer thickness does not lead to a significant improvement - a stabilization of the permeation behavior occurs. In addition to the electrochemical characterization, the evaluation was carried out via the gas-driven variant. This resulted in a permeation reduction factor of up to 150, which confirms a barrier effect. However, it was not possible to confirm the literature values with our coating and the measurement methods used [5].

Gas-driven hydrogen permeation is also ideal for determining the barrier effect of a DLC layer. A PRF of up to 630 was achieved, which means a significant increase compared to ZrN.
The last coating system considered, tungsten carbide, was subjected to a more in-depth examination. The electrochemical measurements presented an excellent barrier effect. Comparing the best value of the amount of charge exchange of the ZrN layers with 1.7mAs with 0.65 mAs at WC, the drastic improvement can be seen. If you compare it to an uncoated reference (see Figure 1**Error! Reference source not found.**), the effect becomes even clearer. While a breakthrough can be seen after around 50min with the uncoated substrate, this is not noticeable after 2h or 68h with the WC-coated sample as illustrated in Figure 2. Furthermore, the hydrogen oxidation current is constantly at a very low level close to zero, which illustrates the strong barrier.

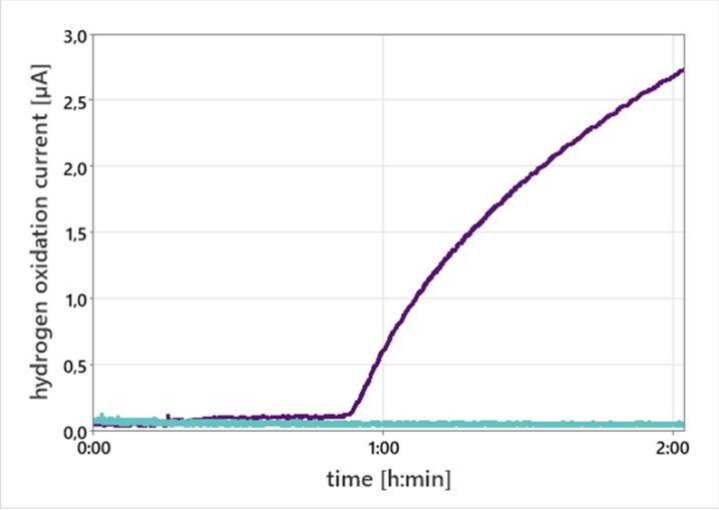

Figure 1: Electrochemical hydrogen permeation measurement on an uncoated steel sample (purple) and a WC-coated sample (turquoise).

DOI: https://doi.org/10.26799/cp-sict-2024

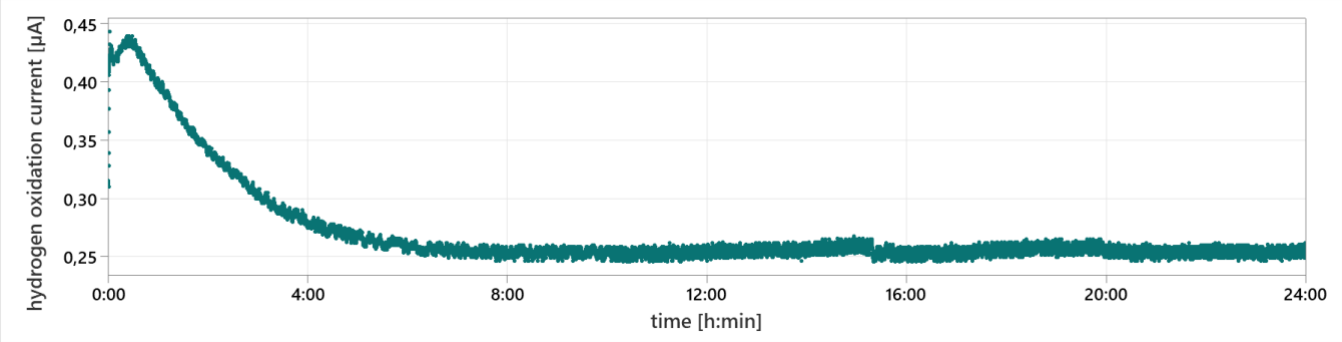

Figure 2: Electrochemical long-time hydrogen permeation measurement on a WC-coated sample.

Analogous to zirconium nitride, the layer thickness influence of tungsten carbide was investigated. The findings of the ZrN coatings could be confirmed. Thin films up to 200 nm have only a low barrier effect. Layer thicknesses from 500 nm show an outstanding hydrogen barrier effect, whereby a further increase of the layer thickness did not result in any significant improvements (**Figure 3**: Comparison of the barrier effect of WC-coated samples of different coating thicknesses (blue: 200nm, red: 500nm, green: 800nm) using electrochemical hydrogen permeation measurement.Figure 3). In order to achieve an optimal layer thickness, further investigations are ongoing.

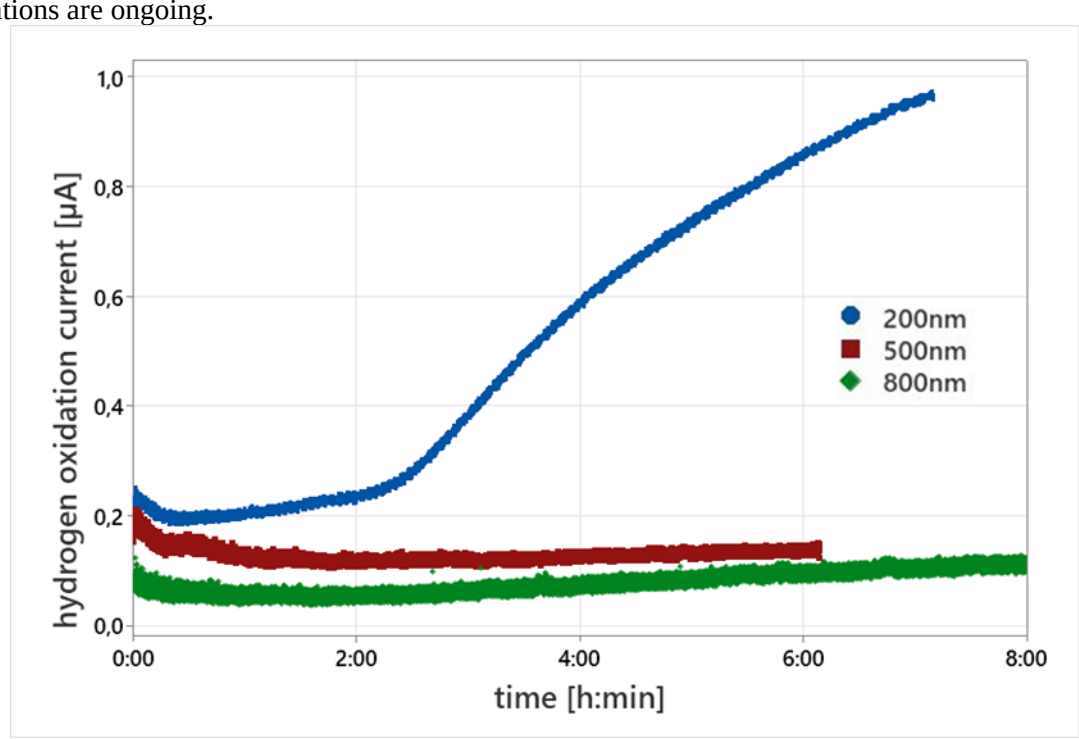

Figure 3: Comparison of the barrier effect of WC-coated samples of different coating thicknesses (blue: 200nm, red: 500nm, green: 800nm) using electrochemical hydrogen permeation measurement.

The promising results from the electrochemical permeation measurements were additionally verified by gas-driven hydrogen permeation. In Figure 4 in an Arrhenius plot, the inverse test temperature is plotted over the steady-state ion current of deuterium. In this way, the barrier effect can be presented clearly, and the permeation reduction factor is determined by the distance between the results of an uncoated reference measurement (black) and the results of the coated samples (coloured) visible. The greater the distance, the higher the barrier effect. Due to the high number of layer variants, a scattering of the results is achieved, which leads to permeation reduction factors in the range of
10^2 to 10^5, but mainly in the range of 10^4-10^5. This indicates an excellent barrier effect, especially under the aspect that the layers were produced in industrial coating machines under conditions of series production and not on an idealized laboratory scale.

DOI: https://doi.org/10.26799/cp-sict-2024

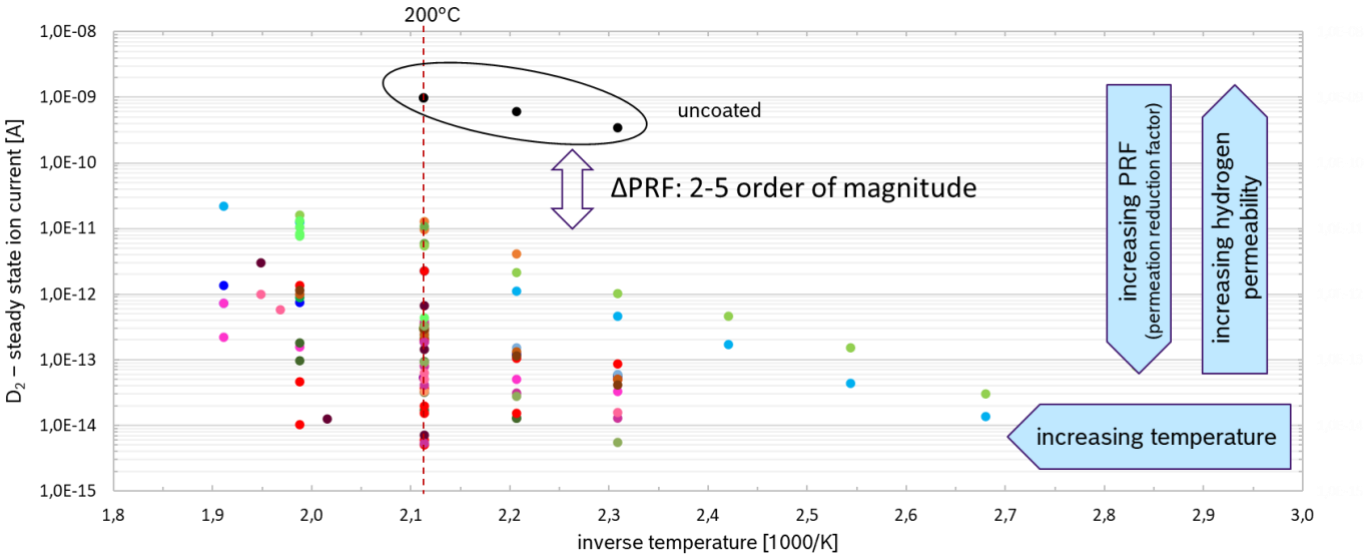

Figure 4: Gas-driven hydrogen permeation measurement on WC-coated samples. Presentation of steady-state ion currents at different temperatures.

4. Conclusion

It has been shown that sputtered coatings are excellent candidates as hydrogen barrier layers for the protection of metallic components. The hydrogen barrier effect depends on various factors. On the one hand, the material composition results in a difference in the operating mechanism and the result. On the other hand, the influence of the layer thickness is particularly significant. This influence is the subject of ongoing investigations in order to determine an optimal layer thickness with regard to barrier effect and economical production. Tungsten carbide stands out with an excellent barrier effect with a permeation reduction factor in the range of 10^4-10^5. Zirconium nitride and DLC also showed a good blocking effect with a PRF of 150 and 630, respectively. The two permeation measurement methods used provided consistent results, hence it would be possible to carry out an evaluation of one of the methods in the future.

References

1. S. K. Bull, « Ab initio screening of refractory nitrides and carbides for high temperature hydrogen permeation barriers", Journal of Nuclear Material, vol. 563, 153611, 2022
2. L. Gröner, « Investigations of the Deuterium Permeability of As-Deposited and Oxidized Ti2AlN Coatings", Materials, vol. 13, no. 9, 2085, 2020
3. iChemAnalytics GmbH. (2020). Flyer Permeation [Online]. Available: https://www.ichemanalytics.de/information/Flyer-Permeation.pdf
4. N.-E. Laadel, « Permeation barriers for hydrogen embrittlement prevention in metals – A review on mechanisms, materials suitability and efficiency", International Journal of Hydrogen Energy, vol. 47, i. 76, pp. 32707-32731, 2022
5. J. Matějíček, "Characterization of less common nitrides as potential permeation barriers", Fusion Engineering and Design, vol. 139, pp. 74-80, 2019
6. V. Nemanič, "Hydrogen permeation barriers: Basic requirements, materials selection, deposition methods, and quality evaluation", Nuclear Materials and Energy, vol. 19, pp. 451-457, 2019
7. B. Zajec, „Hydrogen permeation barrier – Recognition of defective barrier film from transient permeation rate", International Journal of Hydrogen Energy, vol. 36, i. 12, pp.7353-7361, 2011